



Heriot-Watt University
Research Gateway

Flexible Low-Density Polyethylene–BaTiO₃ Nanoparticle Composites for Monitoring Leakage Current in High-Tension Equipment

Citation for published version:

Gupta, R, Badel, B, Gupta, P, Bucknall, DG, Flynn, D & Pancholi, K 2021, 'Flexible Low-Density Polyethylene–BaTiO₃ Nanoparticle Composites for Monitoring Leakage Current in High-Tension Equipment', *ACS Applied Nano Materials*, vol. 4, no. 3, pp. 2413–2422.
<https://doi.org/10.1021/acsnm.0c02719>

Digital Object Identifier (DOI):

[10.1021/acsnm.0c02719](https://doi.org/10.1021/acsnm.0c02719)

Link:

[Link to publication record in Heriot-Watt Research Portal](#)

Document Version:

Publisher's PDF, also known as Version of record

Published In:

ACS Applied Nano Materials

Publisher Rights Statement:

© 2021 The Authors.

General rights

Copyright for the publications made accessible via Heriot-Watt Research Portal is retained by the author(s) and / or other copyright owners and it is a condition of accessing these publications that users recognise and abide by the legal requirements associated with these rights.

Take down policy

Heriot-Watt University has made every reasonable effort to ensure that the content in Heriot-Watt Research Portal complies with UK legislation. If you believe that the public display of this file breaches copyright please contact open.access@hw.ac.uk providing details, and we will remove access to the work immediately and investigate your claim.

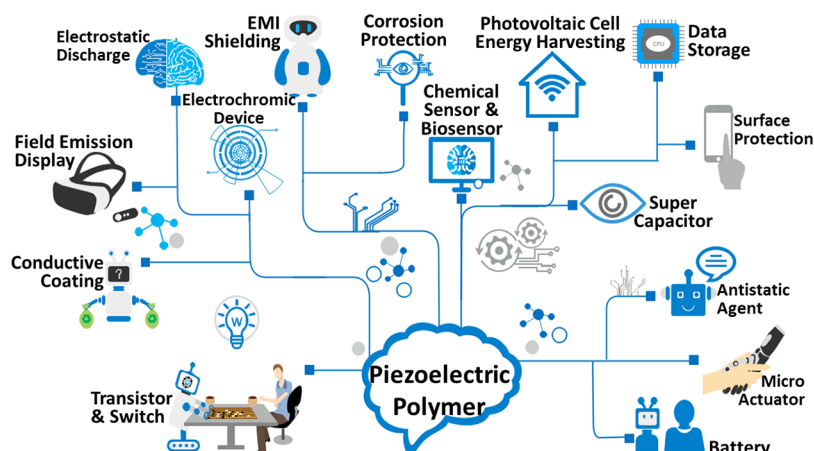


Figure 1. Various emerging application areas of piezoelectric polymer–NP composites.

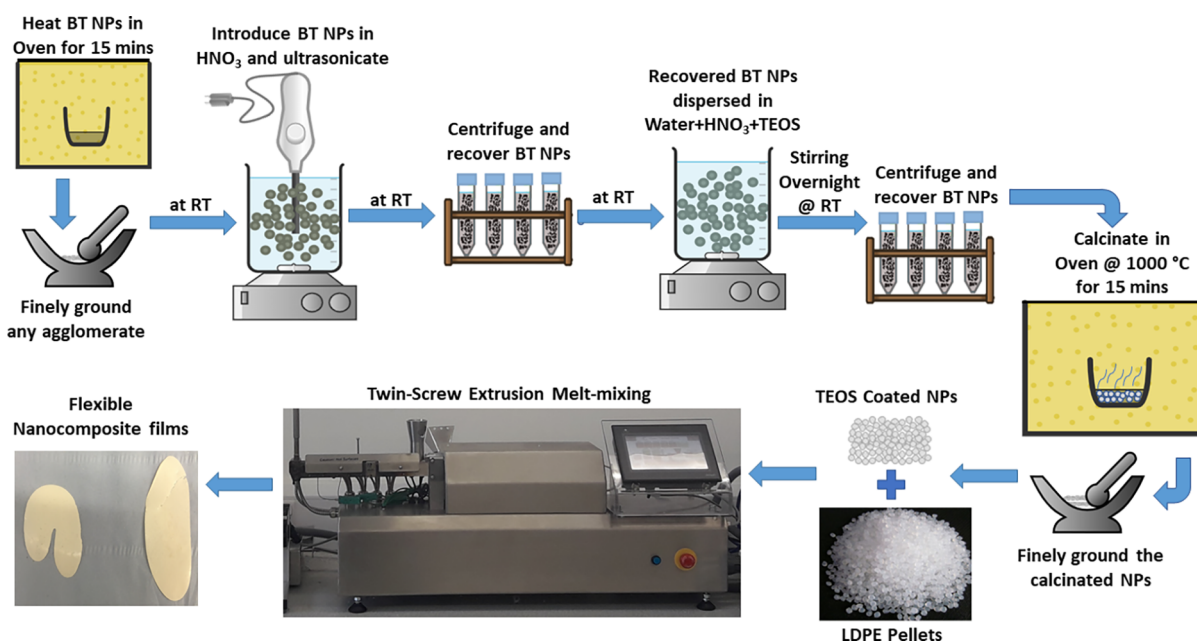


Figure 2. Experimental process followed for the BT NP functionalization and the subsequent flexible polymer–NP composite film samples preparation.

polymer–NP composites causing local charge accumulation and nonuniform electrical or heat conduction.¹⁰ The agglomeration issue can be minimized by various techniques like melt compounding, high shear mixing, three roll mills, solution blending, NP functionalization, and so forth of which functionalization of NPs is the most effective.^{9,11} Functionalization involves coating the individual NP with a chemical moiety that is either the same or compatible with the matrix polymer. The functionalization can serve two purposes, first to reduce the interparticle attraction between the NPs and second to align the NPs hierarchically within the base polymer chain lengths, depending on the functional groups' interactions.

There are many examples of piezoelectric polymer–NP composites with silane–ethanol^{12,13} and oleic acid¹⁴ coatings. Silica coatings using the Stöber method¹⁵ can potentially be a cost-effective and scalable process for commercial NP functionalization manufacturing.^{16,17} Also, silica functionalization of NPs by this method is widely used for producing ultrathin layers,¹⁸ which do not suppress the material properties of the NPs. Hence, the BT NPs, were functionalized employing

the Stöber method in this study. The functionalized NPs dispersed well as compared to the uncoated NPs^{13,19} In this study, barium titanate (BT) NPs are used as they are lead free and cost-effective piezoelectric materials that can be suitable for measuring the strain. As a matrix, the low-density polyethylene (LDPE) was chosen because of its insulating properties and its suitability for application in measuring strain in large high-tension electrical equipment's, wherein the loading is excessively high because of their self-weight like insulated transmission cable lines, umbilicals, and so forth. Moreover, LDPE has a high strength and wide working temperature range of -50 to 85 °C, assuring compliance to a range of industrial applications. LDPE is already widely used as an insulation material in high-voltage DC transmission cables that carry high-voltage DC current²⁰ and offshore umbilicals,²¹ both of which represent a good example of combined high-tension and high-voltage equipment scenario.

EXPERIMENTAL SECTION

Materials. LDPE granules with 2 g/10 min melt flow rate and molecular weight of 45,000 g/mol (density 920 kg/m³) was purchased from Goodfellow (UK). BT (BaTiO₃) NPs (<50 nm size) (BET) having density 6.08 g/mL, 90% technical grade tetraethyl orthosilicate (TEOS), *cis*-cyclooctene containing 100–200 ppm Irganox 1076 FD as an antioxidant, citric acid 99%, and anhydrous 99% heptane were all used as received from Sigma-Aldrich (UK). Other laboratory agents were used as standard.

Experimental Methods. The BT NPs were functionalized/coated as per the following procedures. The pretreatment of BT NPs was performed by dispersing 500 mg of NPs in 10 mL of 1 M HNO₃ and mixed vigorously by ultrasonication for 5 min; this acidic treatment activated the NP surfaces. The supernatant was removed by centrifuging at 4500 rpm and the NPs were subsequently washed three times with deionized water after every centrifuge. The collected NPs were then dispersed in 10 mL of 0.01 M citric acid solution and ultrasonicated for 5 min; the absorption of citric acid enhances the colloidal stability in the alcohol–water mixed solvent, promoting the silica functionalization of NPs. Excess acid was removed by centrifuging at 4500 rpm, followed by washing in deionized water and repeating three times. The collected NPs were then dispersed in 20 mL of water solution containing 20 μ L ammonia and left for 24 h. The silica-coating procedure was implemented by dispersing these citrated BT NPs in 100 mL of a mixed ethanol/water/ammonia solution with 75/23.5/1.5 vol. %, respectively. TEOS¹⁸ (55.5–111 μ L) was then slowly introduced in this solution, which formed ca. 10–15 nm thick silica coatings on the NPs (The uncoated and coated NPs transmission electron microscopy (TEM) images are included in Section S1). The mixture was left overnight at room temperature, this initiated the hydrolysis and condensation of TEOS to form silica shells around the NPs. The silica-coated NPs were then recovered by centrifuging the mixture three times at 5000 rpm for 8 min, followed by ethanol washing each time. The collected BT NPs were then sintered for 3 h, with a gradual rise (5 $^{\circ}$ C/min) in the temperature and finally maintained at 1000 $^{\circ}$ C^{15,22,23} for 15 min to get stable functionalized NPs.

The polymer–NP composites films were then prepared by using a Twin-tech 10 mm twin-screw extruder. 9 wt % of functionalized BT NPs was mixed with 15 g of LDPE along with 0.5 mL *cis*-cyclooctene. The inclusion of *cis*-cyclooctene was the same for the 12 and 15 wt % samples, as it was used considering the weight of LDPE for preventing its oxidation during the extrusion process. All the regions of the extruder were maintained at 140 $^{\circ}$ C temperature and the screw speed set to 60 rpm. To improve the dispersibility of the NPs, the 2 mm diameter extrudate was pelletized under air cooling and extruded a further two times. Finally, the polymer–NP composites films of 80–150 μ m thickness were prepared using a film die attachment having slot area of 80 μ m \times 3 cm. Samples with 12 and 15 wt % of NPs were prepared using the same methodology. The procedure is summarized graphically in Figure 2.

The flexible film samples prepared for the electrical characterization is shown in Figure S1 of Section S1 in the Supporting Information along with the placement of the conductive copper electrodes for the measurement of electrical displacement, current density, and current change under the influence of the applied electric field. The samples are here onward referred as 6, 9, 12, and 15% samples.

Material Characterization. Attenuated total reflection Fourier-transform infrared spectra (ATR–FTIR) were recorded on PerkinElmer Spectrum 100, using a DGS-KBr sensor to identify the effect of the silane functionalization of the NPs. Polymer–NP composites films of thickness around 80–150 μ m were measured and the spectrum was determined from a total of 30 scans in the range of 525–4000 cm^{-1} wavenumber at a resolution of 4 cm^{-1} .

For analyzing the surface characteristics of the functionalized NPs and the dispersion-pattern of NPs in the LDPE matrix TEM images were taken. NPs were dissolved in ethanol (95%, spectrophotometric grade) and a tiny drop of this solution placed on a copper TEM grid and left to air dry, as forced drying induces aggregation of the NPs.

TEM samples of the polymer–NP composites were prepared by microtoming ultrathin sections and placing on 400-mesh-size gilder copper grids; later sputter gold-coated. TEM images were then captured on a Philips CM100 TEM with an accelerating voltage of 100 kV and a spot size of 10 nm, with 0–50 s exposure time. The magnification range of $\times 7900$ to $\times 245,000$ was used to capture images.

Differential scanning calorimetry (DSC) and thermogravimetric analysis (TGA) were performed using TA DSC Q100 and TGA Q500 instruments using a sample mass of 5–12 mg. For DSC, a standard heat/cool/heat cycle analysis was used to evaluate the sample behavior and estimate the T_m for all samples. The process sequence consisted of a ramp heating of 10 $^{\circ}$ C/min from 25 to 150 $^{\circ}$ C, followed by a cooling cycle at 5 $^{\circ}$ C/min to -50 $^{\circ}$ C and finally a heating ramp of 10 $^{\circ}$ C/min back to 150 $^{\circ}$ C. The detailed crystallization calculation method is discussed in Supporting Information S2. The TGA analysis was undertaken with a heating rate of 10 $^{\circ}$ C/min and the total differential weight loss mode was selected to study the thermal behavior of polymer–NP composite samples. Detailed crystallization calculation method is discussed in Section S2 of Supporting Information.

The tensile tests of all the samples were carried out on an Instron 3367 tensile testing machine having a full-scale static rating of ± 30 kN. The sample preparation and testing were undertaken according to the ASTM D3039 standard, with the cross-head displacement set to vary at a rate of 1 mm/min. The test criteria were fixed to 50% change in the maximum load capacity and allowable length extension of 50 mm and change of diameter up to 3 mm.

Thin films with a thickness of around 200 ± 10 μ m were used for measurements of hysteresis loops of electrical displacement versus electric field (D – E), current density (strain) versus electric field, and current versus electric field (I – E) were obtained by using a bespoke setup built using a 33120A Agilent wave generator and TREK 610E amplifier. This is an advanced electrical test system having a piezo sample holder unit connected with a high voltage range of 0 to ± 10 kV amplifier and an output current range of 0 to ± 2000 μ A. The direction of application of the electric field and the direction of displacement (measurement) are maintained the same.

Simulated Model Generation. The TEM images of the PNC samples were processed (details in Section S3 of Supporting Information) and used for the size inputs for the simulated three-dimensional (3D) model using a MATLAB platform. This size data and the percentage weight of the BT NPs loading were then added as the input to the designed MATLAB code to be used as a basis for generating the random NPs/agglomerates in the simulated 3D model of the polymer–NP composites. The code was able to generate the simulated PNC model with the appropriate NP content and diameter sizes passed as the inputs. The black colored spheres in the simulated model represent BaTiO₃ NPs/agglomerates, and their interaction region is represented by the grey region around them.

RESULTS AND DISCUSSION

Characterization Results. The effect that the NP inclusion have on the LDPE matrix is seen in the FTIR spectra, as shown in Figure 3. The polyethylene backbone $-\text{CH}_2$ stretching peaks are seen between 2911 and 2916 cm^{-1} with the stretching of the $-\text{CH}_3$ band around 2839–2849 cm^{-1} (labeled Δ in Figure 4).¹³ Though, these peaks were somewhat suppressed because of the presence of silica functionalization. Additional symbolic peaks of $\nu(\text{C}=\text{O})$, $\delta(\text{C}-\text{H})$, $\gamma(\text{C}=\text{H})$, and $\gamma(\text{C}-\text{H})$ are seen at 1450 cm^{-1} (Θ), 1460 cm^{-1} (Γ), 1030 cm^{-1} (ϑ), and 710 cm^{-1} (\circ), respectively.¹³

The NP bulk absorption (seen at 709–725 cm^{-1})¹⁰ and minor peaks around 1030–1060 cm^{-1} (π) are because of the Si–O stretching of SiOH,¹⁹ whereas the peak at 862 cm^{-1} is because of the hydroxyl (OH) group of the adsorbed H₂O.²⁴

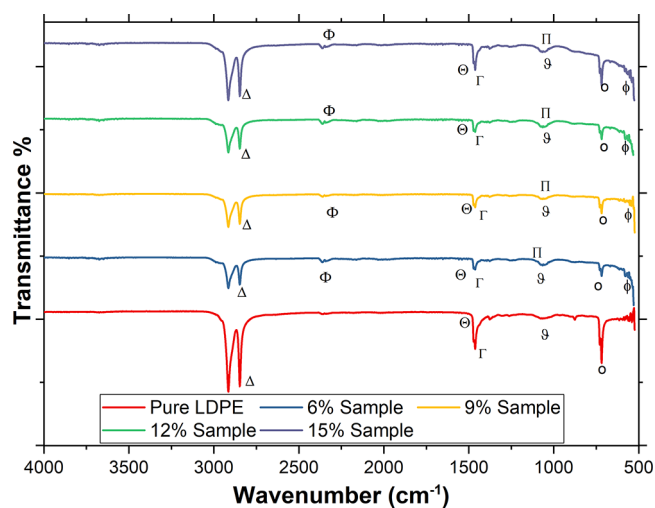


Figure 3. FTIR spectra of pure LDPE and the prepared 6, 9, 12, and 15% polymer–NP composite samples. Representative peaks are Δ - ν (C–H), Θ - ν (C=O), Γ - δ (C–H), ϑ - γ (=C–H), and \circ - γ (C–H) for LDPE stretch bonds; π (Si–O–Si) of Silica; Φ -BaCO₃ and ϕ -TiO from BaTiO₃.

The BaCO₃ (Φ) and TiO (ϕ) bonds from the BaTiO₃ NPs are observed around 2260 and 530 cm⁻¹, respectively.¹⁰

The suitability of the synthesized material for flexible sensing applications can only be realized by the feasibility of their film-forming capability. The degree of crystallinity dictates the suitability of the polymer–NP composite material for film formability or its use in structural applications.^{8,25} From Figure 4a, it is observed that the melting temperature (T_m) decreases with the increased NP loading, as expected with the introduction of dielectric filler impurities that have higher thermal and electrical affinity.¹³ Though the higher loading of BT NPs also induce higher heat absorbing capacity within the polymer–NP composite samples but here the resulting reduction in the degree of crystallinity brings the subsequent T_m of 12% sample as almost similar to that of the pure LDPE sample. Table S1 in Section S2 of the Supporting Information summarizes the important results from the DSC data with the percentage crystallinity calculated from the heat of enthalpy of the melt peak assuming that fully crystallized polyethylene has a heat of enthalpy of 286.7 J/g.¹³ The degree of crystallinity of all the samples were calculated using the equation mentioned in Section S2.

Reduced polymer chain mobility causes slow crystal formation and hence results in a higher degree of crystallinity.⁸ Increasing crystallinity leads to induced properties of which the most significant ones in this study are the charge carrying capacity and mechanical stability. However, here the

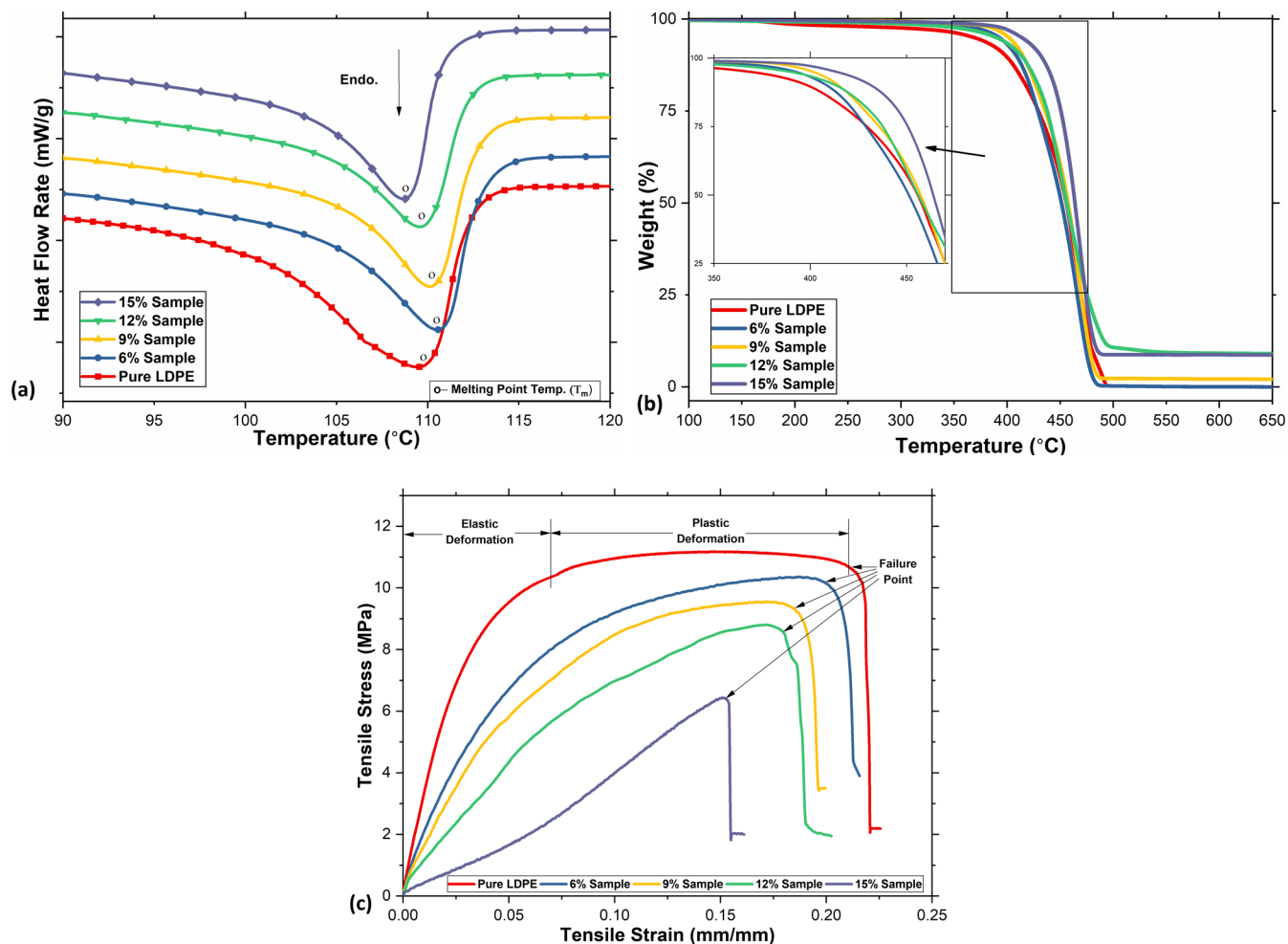


Figure 4. (a) DSC melting endothermic peaks used for degree of crystallinity calculation, (b) TGA data plots, and (c) tensile stress vs tensile strain plots for the pure LDPE and the prepared 6, 9, 12, and 15% polymer–NP composite samples.

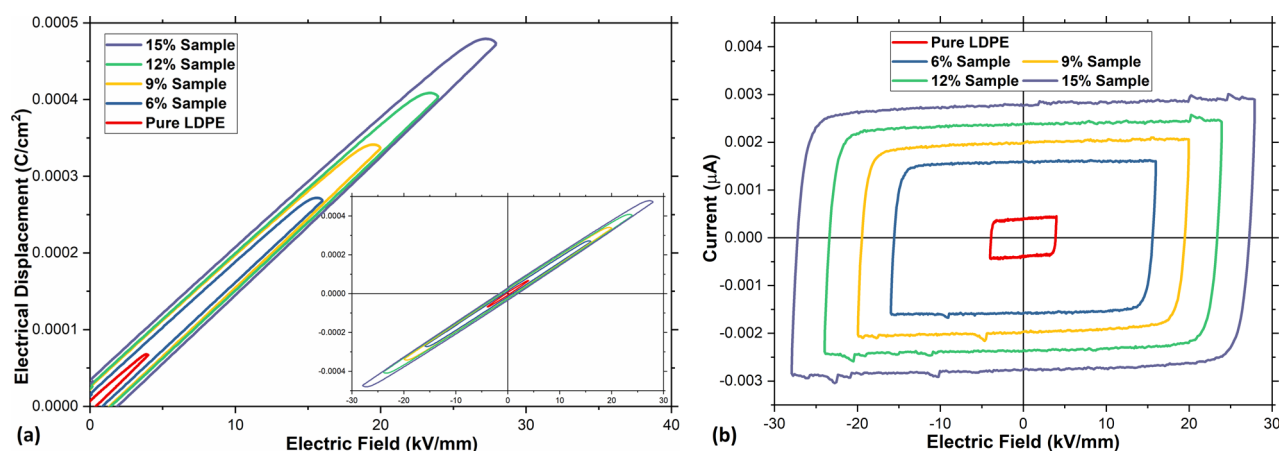


Figure 5. (a) Electrical displacement versus electric field (D – E) hysteresis loops and (b) current vs electric field (I – E) curves for pure LDPE and the prepared 6, 9, 12, and 15% polymer–NP composite samples.

decreasing trend of degree of crystallinity with the increasing NP loading is because of the impurities introduced by NP inclusion that correspondingly resulted in the observed T_m reduction. This confirms that the synthesized samples can be processed into thin films akin to a pure LDPE material. The melting onset temperature of the 6 and 9% samples were seen to be higher than that of the pure LDPE because of the oxide inclusions of BT NPs, which can withstand higher temperatures. However, as the content of the NPs is increased further to 12 and 15 wt %, the heat absorbing capacity is no doubt increased further, but the reduced polymer weight tends to melt more easily. In addition, the BT NPs in 12 and 15% samples are more agglomerated (as seen from the TEM analysis and 3D modeling), leading to local energy absorption.

The effect due to silane functionalization on the thermal response of the samples is studied by the TGA analysis, as presented in Figure 4b, it displays the thermally degrading performance of all the prepared polymer–NP composite samples and in comparison with the pure LDPE sample. The pure LDPE sample revealed the degrading commencement at around 170 °C, as observed in Figure 6. On the contrary, the polymer–NP composite sample having the lowest content of BT NPs (viz. 6% sample) revealed the onset degradation behavior almost 70 °C greater than that for the pure LDPE sample. This is apparent because of the oxide additions by the BT NPs, which exhibit ceramic qualities and can withstand higher temperatures themselves. Additionally, as the wt % of the BT NPs was increased there was a gradual improvement in the onset of degradation temperature of the polymer–NP composite samples; however, the 15% sample showed the highest temperature for the degradation onset. Which can be attributed solely because of the highest BT NP concentration. BT NPs are well known for their ceramic behavior, though the heat-steady response herein is linked to the limited oxygen availability and because of the potential volatile species adsorption after the degradation commenced.¹³ As observed from the DSC study, there was a decrease in the degree of crystallinity with the increase in the wt % of BT NPs for all the polymer–NP composite samples prepared, but the superior dispersion because of the result of silane functionalization additionally enhanced the stable thermal response of the polymer–NP composite samples.

The mechanical properties in terms of the film processing capability of the polymer–NP composite samples were studied

as response of their flexibility through tensile testing. As observed from Figure 4c, all the samples showed an initial linear region of elastic deformation but not all samples showed a plastic deformation region. This was most obvious in the 15% sample. It is pertinent that the plastic behavior of LDPE is gradually decreased with the increase of the nanoinclusion loading in the polymer–NP composite sample.²⁶ Hence, it is important to determine an optimum limit of the NP loading wt % to get the bespoke polymer–NP composite, beyond which the plastic behavior will eventually be lost.²⁷ In this study, it is seen that as the wt % of NP loading is increased there is a gradual loss in the plastic deformation region of the polymer–NP composite samples. It is observed that the 6 and 9% samples showed quite a comparable response in terms of the plastic deformation region as with the pure LDPE sample, though the 12% sample showed a reduced amount of plastic deformation. However, the maximum loss is observed in the 15% sample, this can be attributed partly because of the higher content of NPs and the resulting possibilities of agglomeration sites because of the increased interaction among the NPs at such higher loadings.¹³ The 12% sample shows a sufficient degree of plastic deformation, but the response of the 15% sample is almost like a brittle failure. Therefore, among all the prepared samples, the 12% loading of NPs is the practical limit for flexible film samples for the sensing applications as studied herein.

Figure 5a shows the D – E hysteresis loops for pure LDPE and the prepared polymer–NP composite samples (6, 9, 12, and 15% samples). The maximum electrical displacement shown by the polymer–NP composite sample of 6, 9, 12, and 15% BT NP variations was 2.727×10^{-4} , 3.424×10^{-4} , 4.098×10^{-4} , and 4.802×10^{-4} C/cm², respectively. These are all larger than that for the pure LDPE of 6.875×10^{-5} C/cm². The drastic increase in conduction with the higher dielectric content of the BT NPs proves the improvements with the loading of the NP inclusion. The increase in the maximum displacement (D_{\max}) is primarily because of the inclusion of BT NPs, which possibly caused the decrease in volume of the doped conductive composites. Also, as the wt % of the NPs increases there is a possibility of some reduction in the electrical displacement or polarization per unit volume because of the random orientations of the local polar domains in NPs as reported in the literature.²⁸ This is also a possible reason

why there is not much of a difference observed in the response ratio of 12 and 15% samples.

The current versus electric field behavior, as shown in Figure 5b, is used for the coercive field measurements (which is also obtained using the electrical displacement loops). On application of the electric field, the current signal behaviors are observed from the polymer–NP composite materials viz. leakage current.^{29,30} In Figure 5b, the current peaks are visible for all samples as observed in a similar study.²⁹ The peak current values observed for the 6, 9, 12, and 15% NP composite samples are 0.0016, 0.0021, 0.0025, and 0.0029 μA , respectively. These values are an order of magnitude larger than the very small response seen for a pure LDPE of 0.00045 μA . The magnitude of the current peaks increases proportionally with the increasing NP loading in the sample, which can be attributed to the insulating behavior of the nanocomposite. The nature of variation in maximum values because of the applied electric field is very low because the applied field was never increased to above the breakdown value.

It can also be seen from Table 1 that the coercive field I_c (the field which is necessary to turn the remnant displacement

Table 1. Maximum Current I_{max} , Remnant Current I_r , and Coercive Field I_c for pure LDPE and the Prepared 6, 9, 12, and 15% Polymer–NP Composite Samples

sample	I_{max} (μA)	I_r (μA)	I_c (kV/mm)	I_r/I_{max}
pure LDPE	4.5×10^{-4}	3.7×10^{-4}	3.8	0.82
6% sample	16.5×10^{-4}	15.3×10^{-4}	15.6	0.93
9% sample	21.0×10^{-4}	19.6×10^{-4}	19.5	0.94
12% sample	24.9×10^{-4}	23.5×10^{-4}	23.3	0.94
15% sample	29.4×10^{-4}	27.7×10^{-4}	27.2	0.94

to zero or flipping it) and the remnant current I_r increases with increasing NP concentration. This is in line with the response observed with I_{max} . This observed behavior demonstrates an increased strength of electrical displacement with an applied electric field in the synthesized film samples, which is a desirable quality for any sensing application.³⁰

The changes in current density of the prepared polymer–NP composites thin-film samples as a function of the applied electric field were also studied (Figure 6) to estimate the extent to which the BT polymer–NP composite can polarize and show higher current density response acting as superior capacitor materials. The results show an enhanced current density response alongside the changes in the electrical field with increasing BT NP loading, which clearly hints that pure LDPE can only perform until ca. 25 kV/mm field and is unsuitable for higher current density response. This response trend is similar to energy density variation under the influencing applied electric field³¹ and is many times studied for estimating the energy holding or capacitor-material suitability of such polymer–NP composites. Figure 6 shows the trend of the increasing current density with the increase of the applied electric field as observed in previous studies with BT crystals.³² The results suggest that the current density shows a stable linear response to the applied electric field, which is a key requirement for sensing purposes. This comparison plot in Figure 6 suggests that the polymer–NP composite sample having more NPs can transfer the applied energy to BT NPs more efficiently or vice versa.³³

The films show a decrease in strain, and hence, a corresponding increase in the current density with the increase

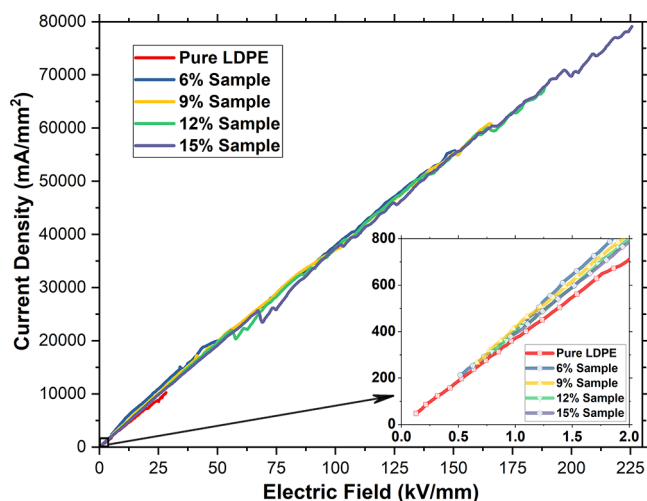


Figure 6. Current density vs electric field measurements for pure LDPE and the prepared 6, 9, 12, and 15% polymer–NP composite samples.

in NP loading and applied electric field.²⁹ This capability of variation in current density (strain) limits with the changing NP wt % loading is suitable to be used for sensing applications. The sample with 12% ($6.7496 \times 10^4 \text{ mA/mm}^2$) and 15% ($7.9573 \times 10^4 \text{ mA/mm}^2$) NP loading showed a huge difference in the current density values as compared to the pure LDPE sample ($1.0525 \times 10^4 \text{ mA/mm}^2$); and similar response was also observed in the previous $D-E$ measurements. Though the trend was proportional to the NP loading in each polymer–NP composite samples from 6 to 15% samples. All the samples showed a response starting just above zero, signifying that because of their piezoelectric nature the BT NPs only start responding above a certain threshold of the applied electric field. The higher loading of NPs involve more energy to be applied to overcome the threshold, raising the responding limit barrier;^{31,34} viz. observed as the increment in the starting position of the response for each polymer–NP composite samples with increasing NP loading. The application of such polymer–NP composite materials can be exploited in high voltage applications, for example, in HVDC cable transmission lines, the asset integrity becomes a major challenge as various failure modes often depend upon the structure.³⁵ The cyclic fatigue failure caused by the inverting compressive and tensile loading on such cables can be detected by implementing such designed polymer–NP composite materials in key regions of asset deployment, as part of the successful remote prognostic effort.

Simulated Model Generation Showing IR. The TEM images of all the polymer–NP composite samples are shown in Figure S4 of Section S1 in the Supporting Information. As seen from these TEM images, the agglomeration of the BT NPs increases with their increased loading. The TEM image of a sample containing the uncoated BaTiO_3 NP sample was also taken and highlights the improvement that the silica functionalization makes to the NP dispersion (see Section S1). The size of agglomerates in 15% sample are much larger than the other samples. It is clear that at a higher loading the NPs are in close proximity with each other, and the dipole–dipole interaction between them causes the issue of agglomeration. The analysis of the TEM images was done using image processing package, ImageJ, and the measurement tool option for ferret diameter was used to approximate the

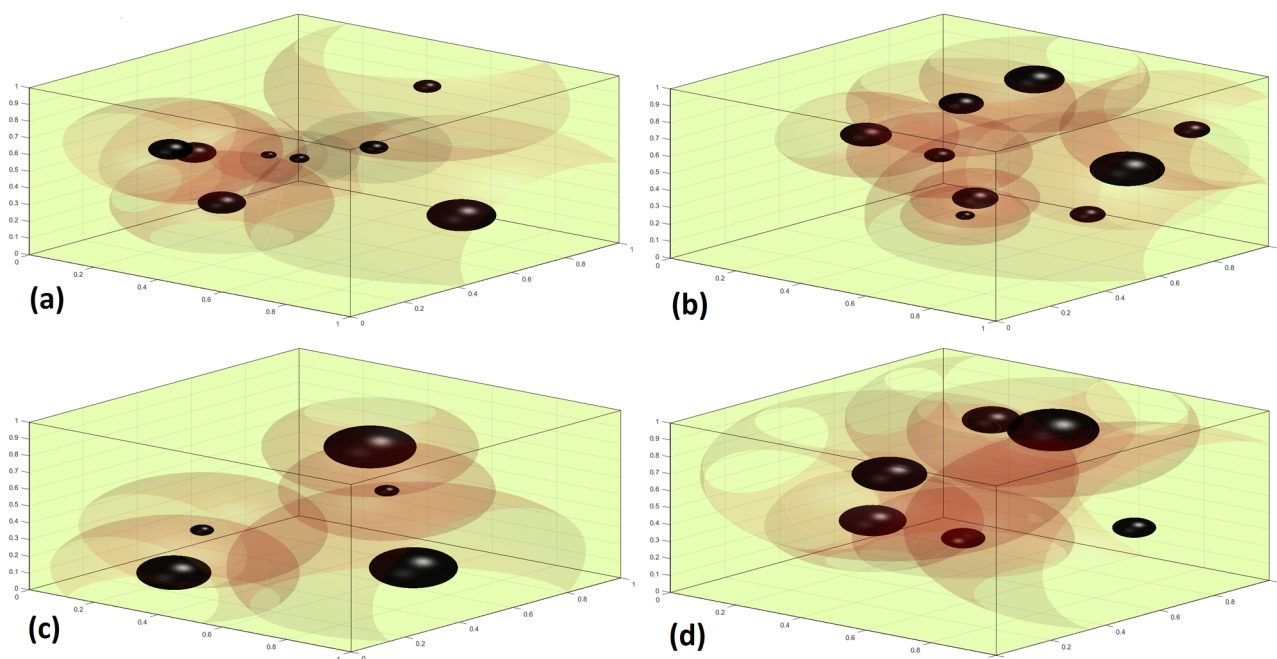


Figure 7. Simulated model representation showing the IR region of the individual NP/agglomerate present in the synthesized polymer–NP composite (1 cubic micrometer size) samples with varying wt % of NP loading, wherein (a) 6% sample, (b) 9% sample, (c) 12% sample, and (d) 15% sample.

designated region of the NP/agglomerate referred as an ellipsoid unit. The diameter range was calculated for individual NP and the biggest agglomerate present, based on the relation of $\sqrt{(\text{minFeret} \times \text{maxFeret})}$ (where minFeret and maxFeret are the minimum and maximum Feret diameters as calculated by ImageJ). The calculated diameter range for each sample from this study are summarized in Table S2 of Section S3 in Supporting Information. The values from Table S2 of Section S3 in Supporting Information were utilized for inputting to the designed MATLAB code that created the simulated 3D model of the polymer–NP composites with NP/agglomerates represented as spherical entities. To minimize the intricacy of the generated 3D model, all the NPs/agglomerate units were created as spherical entities. It is shown in Figure S5 of Section S3 of the Supporting Information.

The aim of generating the simulated model was to visualize and infer the NPs/agglomerate dispersion state in the synthesized composites having different wt % concentrations of the NPs and to inter-relate it with the electrical measurements, which otherwise is fairly difficult to do with the physical characterization methods. The interaction radius (IR), which is the nearest distance among the generated spheres (neighbors), was also calculated when the simulated model was generated. The interaction region or the influencing region of each sphere representing the NP/agglomerates was understood by the calculated IR values. The interaction among the NPs, that is, charged electron transfer among them or their conductive/insulating nature are defined by two main constraints viz. the dispersion state and the IR value.¹³ Hence, studying the dispersion state with the help of the simulated model is an important prospect. The generated IR values are included in Table S3 in Section S3 of Supporting Information, using which the interaction region was graphically represented, as shown in Figure 7.

The interaction region or IR of each NP/agglomerate is first dependent on its own size and then the arrangement of its

nearest neighbor NP/agglomerate. In this study, the calculated IR values were found to increase from ca. 275 to 310 nm with increase in the concentration of BT NPs in polymer–NP composite samples of 6 to 12%, but then it drops to 300 nm for 15% sample. This change in trend can be studied from the simulated models, as shown in Figure 7, which clarifies that the 12 and 15% samples include more agglomerated regions. This suggests that higher BT NP content is unsuitable for polymer–NP composite preparations, as the functionalization of NPs can also be ineffective in such instances. With the largest sized agglomerates (see Table S2 in Section S3 of Supporting Information), the sample with 15% sample NPs showed the second highest calculated IR value after the 12% sample. The lowest calculated IR value observed in the 6% sample is the most desirable. This ensures that the charge transfer/interaction between the NPs can be easily executed because of their proximity and homogeneous dispersion. Hence, it can be concluded that the polymer–NP composite's performance is directly related to the NP dispersions, and higher NP loading may not necessarily produce optimal performance enhancement.

Relating the overall studied parameters of all the samples, as summarized in Table 2 below, it can help concluding the suitable choice of the polymer–NP composite material for the sensor application.

Although the LDPE has a tendency for current leakage at high applied electric fields, because of the BT nanoinclusions, it also starts exhibiting increased current density response, which aids in the precision of sensibility. This improvement is proportional with the BT loading in the sample, but on the other hand, the highest loading of NPs has shown to reduce the flexibility and the degree of crystallinity of the sample. Although it is observed that as the loading of NPs increases the magnitude of the leakage current at the maximum applied electric field also increases, the critical loading of NPs is not the only consideration. The uniform dispersion of NPs can

Table 2. Comparison Table of the Key Parameters Studied for All the Samples

sample	degree of crystallinity (%)	I_r/I_{max}	current density (mA/mm ²)	IR (nm)
pure LDPE	39 ± 1	0.82	1.1 × 10 ⁴	n/a
6% sample	38 ± 2	0.93	5.6 × 10 ⁴	275
9% sample	36 ± 1	0.94	6.1 × 10 ⁴	290
12% sample	34 ± 1	0.94	6.7 × 10 ⁴	310
15% sample	33 ± 1	0.94	8.0 × 10 ⁴	300

make a significant difference,^{36–38} which may result in a lower value of IR, that is, quicker interaction between the NPs in terms of electron transfer, and hence, the role of involving effective functionalization technique can be critical in defining the electro-mechanical response of the polymer–NP composite samples. The capability of the prepared polymer NP composite samples for the leakage current density increases from 1.1 × 10⁴ mA/mm² of LDPE to 6.7 × 10⁴ and 8.0 × 10⁴ mA/mm² for the higher NP loading in 12 and 15% samples, which is *ca.* 5 times and 6 times increase, respectively. Another study involving different vol % loadings of BT nanofillers showed improvement of 12 times for 3.6 vol % of the BT nanofillers as compared to pure biaxially oriented polypropylene.³⁹ Though the prepared samples in this study showed a much higher change in the current density as compared to other polymer–NP studies, wherein the prepared polyvinylidene fluoride nanocomposite samples with 3 vol % did not show much difference in the leakage current density response, mostly because it did not involve dielectric NPs like BT.⁴⁰ This also confirms that the suitable choice of NPs is also important for improving the current density response and for tuning the designed polymer NP composites. Further, the inter-relation of electrical measurements with the crystallinity study suggests that though higher NP loading in the synthesized polymer–NP composite can provide improved a sensing response with even slight variations but that itself can limit the formation of thin films desired for flexible sensing applications because of the degrading degree of crystallinity. In addition, the dispersion state of NPs is overall much better in 6% sample but almost similar for 12 and 15% samples. Hence, the 12% sample is ideally suited for high current density applications, considering the overall trade-off between mechanical property, electrical property, and NP dispersibility.

CONCLUSIONS

The prepared BaTiO₃–polyethylene NP composite samples have showed an interestingly insulating behavior instead of the anticipated ferroelectric (pyro/piezoelectric) response. FTIR results have revealed changes to LDPE backbone conformations and the effect due to silica coating on BaTiO₃ NPs. The melting temperature and the degree of crystallinity of the polymer NP composite samples decreased with the increased NP loading. The highest change in the degree of crystallinity was observed for the samples containing 15% NPs, which also resulted in the reduction of toughness as observed in the tensile test measurements. The electrical displacement versus electric field (D – E) measurements and the maximum displacement (D_{max}) and coercive field (D_c) showed the insulating behavior for the resulting polymer–NP composite samples. The direct linear relation between the current density

(uniform strain) values and applied electric field has confirmed the suitability of the polymer–NP composite for high electric density sensing. Overall, in terms of the physical properties (T_g , degree of crystallinity, onset degradation temperature, and tensile test data), electrical properties (electrical displacement, leakage current, and current density), and the dispersion state attained, the results suggest that the 12% polymer–NP composite sample is the most desirable for flexible sensor applications. Such polymer–NP composite materials could be exploited as a combined insulator and sensing medium for the high-tension and high-voltage scenarios.

ASSOCIATED CONTENT

Supporting Information

The Supporting Information is available free of charge at <https://pubs.acs.org/doi/10.1021/acsnm.0c02719>.

Prepared film sample and their testing setup is included in Section S1 of Supporting Information, TEM images of the uncoated and silica-coated BaTiO₃ NPs along with the TEM images of the uncoated BaTiO₃ polymer NP sample and all the polymer–NP composite samples, details of the method followed for the degree of the crystallinity measurement using the DSC data and the key observations from the DSC plot and the calculated degree of crystallinity is included in Section S2 of Supporting Information, estimates of the NP/agglomerate's sizes from all the processed TEM images for all the polymer–NP composite sample variations, and simulated 3D model of the polymer NP composite with NP/agglomerates represented as spherical entities along with the calculation of their calculated IR (PDF)

AUTHOR INFORMATION

Corresponding Authors

Ranjeetkumar Gupta – School of Engineering & Physical Sciences and Smart Systems Group, Institute of Sensors, Signals and Systems, Heriot-Watt University, Edinburgh EH14 4AS, U.K.; orcid.org/0000-0001-5647-0691; Email: r.gupta@hw.ac.uk

Ketan Pancholi – School of Engineering, Robert Gordon University, Aberdeen AB10 7AQ, U.K.; orcid.org/0000-0001-7662-7764; Email: k.pancholi2@rgu.ac.uk

Authors

Birzhan Badel – School of Engineering, Robert Gordon University, Aberdeen AB10 7AQ, U.K.

Priya Gupta – Department of Electrical and Electronics Engineering, LNCTS, Indore 453111, India

David G. Bucknall – School of Engineering & Physical Sciences, Heriot-Watt University, Edinburgh EH14 4AS, U.K.; orcid.org/0000-0003-4558-6933

David Flynn – School of Engineering & Physical Sciences and Smart Systems Group, Institute of Sensors, Signals and Systems, Heriot-Watt University, Edinburgh EH14 4AS, U.K.

Complete contact information is available at: <https://pubs.acs.org/10.1021/acsnm.0c02719>

Notes

The authors declare no competing financial interest.

ACKNOWLEDGMENTS

The authors are grateful to the staff of School of Engineering (David Howie, Alan Mclean, Alexander Laing, David Smith, Martin Johnstone, Alan Macpherson, Patrick Kane, and the EA Team), School of Pharmacy (Laurie Smith, Tracy Willox, Bruce Petrie, Carlos Fernandez, Jenny Macaskill, and Kerr Mathews) at Robert Gordon University and Nathan Oo (EPS) of Heriot-Watt University for making their facility available for part of this research. Financial support is also provided by Innovate UK, Heriot-Watt University and MacTaggart, Scott & Co. Ltd. through KTP grant reference no. 11746.

REFERENCES

- (1) Bai, Y.; Cheng, Z.-Y.; Bharti, V.; Xu, H. S.; Zhang, Q. M. High-dielectric-constant ceramic-polymer composites. *Appl. Phys. Lett.* **2000**, *76*, 3804–3806.
- (2) Mitrakos, V.; Hands, P.; Cummins, G.; Macintyre, L.; Denison, F.; Flynn, D.; Desmulliez, M. Nanocomposite-based microstructured piezoresistive pressure sensors for low-pressure measurement range. *Micromachines* **2018**, *9*, 43.
- (3) Kaufmann, J. G.; Flynn, D.; Brown, K.; Desmulliez, M. P. Agile MEMS packaging for mass customized MEMS products. *2011 Symposium on Design, Test, Integration & Packaging of MEMS/MOEMS (DTIP)*, 2011; pp 41–45.
- (4) Collins, R. *Multifunctional Composites 2019–2029: Technology, Players, Market Forecasts*, 2019.
- (5) Tan, Q. C.; Shanks, R. A.; Hui, D.; Kong, I. Functionalised graphene-multiwalled carbon nanotube hybrid poly (styrene-butadiene-*b*-styrene) nanocomposites. *Composites, Part B* **2016**, *90*, 315–325.
- (6) Safdari, M.; Al-Haik, M. S. A Review on Polymeric Nanocomposites: Effect of Hybridization and Synergy on Electrical Properties. *Carbon-Based Polymer Nanocomposites for Environmental and Energy Applications*; Elsevier, 2018; pp 113–146.
- (7) Ng, J. H.; Ssekitooleko, R. T.; Flynn, D.; Kay, R. W.; Démoré, C. E.; Cochran, S.; Desmulliez, M. P. Design, manufacturing and packaging of high frequency micro ultrasonic transducers for medical applications. *2011 IEEE 13th Electronics Packaging Technology Conference*, 2011; pp 93–98.
- (8) Gupta, R.; Huo, D.; White, M.; Jha, V.; Stenning, G. B. G.; Pancholi, K. Novel Method of Healing the Fibre Reinforced Thermoplastic Composite: A Potential Model for Offshore Applications. *Compos. Commun.* **2019**, *16*, 67–78.
- (9) Gupta, R.; Pancholi, K.; De Sa, R.; Murray, D.; Huo, D.; Droubi, G.; White, M.; Njuguna, J.; Njuguna, J. Effect of Oleic Acid functionalised Iron Oxide Nanoparticles on Properties of Magnetic Polyamide-6 Nanocomposite. *JOM* **2019**, *71*, 3119–3128.
- (10) Gupta, R.; Huo, D.; Pancholi, M.; Njuguna, J.; Pancholi, K. Insulating polymer nanocomposites for high thermal conduction and fire retarding applications. *The Proceedings of the 3rd Defence & Security Doctoral Symposium 2017*, 2017.
- (11) Gupta, R.; Pancholi, K.; Prabhu, R.; Pancholi, M.; Huo, D.; Jha, V.; Latto, J. Integrated self-healing of the composite offshore structures. *OCEANS 2017-Aberdeen*, 2017; pp 1–4.
- (12) Phan, T. T. M.; Chu, N. C.; Luu, V. B.; Nguyen Xuan, H.; Pham, D. T.; Martin, I.; Carrière, P. Enhancement of polarization property of silane-modified BaTiO₃ nanoparticles and its effect in increasing dielectric property of epoxy/BaTiO₃ nanocomposites. *J. Sci. Adv. Mater. Dev.* **2016**, *1*, 90–97.
- (13) Gupta, R.; Smith, L.; Njuguna, J.; Deighton, A.; Pancholi, K. Insulating MgO-Al₂O₃-LDPE Nanocomposites for Offshore Medium Voltage DC Cable. *ACS Appl. Electron. Mater.* **2020**, *2*, 1880–1891.
- (14) O'Brien, S.; Brus, L.; Murray, C. B. Synthesis of monodisperse nanoparticles of barium titanate: toward a generalized strategy of oxide nanoparticle synthesis. *J. Am. Chem. Soc.* **2001**, *123*, 12085–12086.
- (15) Park, J. S.; Han, Y. H. Nano size BaTiO₃ powder coated with silica. *Ceram. Int.* **2005**, *31*, 777–782.
- (16) Wong, Y. J.; Zhu, L.; Teo, W. S.; Tan, Y. W.; Yang, Y.; Wang, C.; Chen, H. Revisiting the Stöber method: inhomogeneity in silica shells. *J. Am. Chem. Soc.* **2011**, *133*, 11422–11425.
- (17) Zhang, Y.; Cao, M.; Yao, Z.; Wang, Z.; Song, Z.; Ullah, A.; Hao, H.; Liu, H. Effects of silica coating on the microstructures and energy storage properties of BaTiO₃ ceramics. *Mater. Res. Bull.* **2015**, *67*, 70–76.
- (18) Kralj, S.; Makovec, D.; Čampelj, S.; Drofenik, M. Producing ultra-thin silica coatings on iron-oxide nanoparticles to improve their surface reactivity. *J. Magn. Magn. Mater.* **2010**, *322*, 1847–1853.
- (19) Mornet, S.; Elissalde, C.; Hornebecq, V.; Bidault, O.; Duguet, E.; Brisson, A.; Maglione, M. Controlled growth of silica shell on Ba_{0.6}Sr_{0.4}TiO₃ nanoparticles used as precursors of ferroelectric composites. *Chem. Mater.* **2005**, *17*, 4530–4536.
- (20) Andersson, M. G.; Hynynen, J.; Andersson, M. R.; Englund, V.; Hagstrand, P.-O.; Gkourmpis, T.; Müller, C. Highly insulating polyethylene blends for high-voltage direct-current power cables. *ACS Macro Lett.* **2017**, *6*, 78–82.
- (21) Donnison, C.; Dutton, A. Umbilical for Offshore/Reduction of Hydrocarbons. U.S. Patent 20060144456A1, 2006.
- (22) Suzuki, N.; Zakaria, M. B.; Torad, N. L.; Wu, K. C.-W.; Nemoto, Y.; Imura, M.; Osada, M.; Yamauchi, Y. Synthesis of Highly Strained Mesostructured SrTiO₃/BaTiO₃ Composite Films with Robust Ferroelectricity. *Chem.—Eur. J.* **2013**, *19*, 4446–4450.
- (23) Tong, Y.; Talebinezhad, H.; Lu, X.; Cheng, Z.; Hill, C.; Tucker, D. Microstructure and enhanced dielectric properties of BaTiO₃-SiO₂ nanocomposites using hydrogen treated nanoparticles. *IET Nanodielectrics* **2019**, *2*, 41–47.
- (24) Prescott, H. A.; Li, Z.-J.; Kemnitz, E.; Deutsch, J.; Lieske, H. New magnesium oxide fluorides with hydroxy groups as catalysts for Michael additions. *J. Mater. Chem.* **2005**, *15*, 4616–4628.
- (25) Gupta, R.; Staknevcicius, R.; Pancholi, K. Rapid Multifunctional Composite Part Manufacturing using Controlled In-situ Polymerization of PA6 Nanocomposite. *Procedia CIRP* **2019**, *85*, 61–65.
- (26) Carotenuto, G.; De Nicola, S.; Palomba, M.; Pullini, D.; Horwell, A.; Hansen, T. W.; Nicolais, L. Mechanical properties of low-density polyethylene filled by graphite nanoplatelets. *Nanotechnology* **2012**, *23*, 485705.
- (27) de Oliveira, A. D.; Beatrice, C. A. G. Polymer nanocomposites with different types of nanofiller. *Nanocomposites—Recent Evolutions*; IntechOpen, 2018; pp 103–104.
- (28) Kshirsagar, S. H.; Tarale, A. N.; Jigajeni, S. R.; Salunkhe, D. J.; Joshi, P. B. Effect of Ni doping on ferroelectric, dielectric and magneto dielectric properties of strontium barium niobate ceramics. *Indian J. Pure Appl. Phys.* **2015**, *53*, 119–124.
- (29) Chen, J.; Wang, Y.; Xu, X.; Yuan, Q.; Niu, Y.; Wang, Q.; Wang, H. Ultrahigh discharge efficiency and energy density achieved at low electric fields in sandwich-structured polymer films containing dielectric elastomers. *J. Mater. Chem. A* **2019**, *7*, 3729–3736.
- (30) Kumar, A.; Prasad, V. B.; Raju, K. J.; James, A. Optimization of poling parameters of mechanically processed PLZT 8/60/40 ceramics based on dielectric and piezoelectric studies. *Eur. Phys. J. B* **2015**, *88*, 287.
- (31) Yu, J.; Ding, S.; Yu, S.; Lu, Y.-C.; Xu, P.; Chu, B.; Sun, R.; Xu, J.; Wong, C.-P. Nanoparticles with rationally designed isoelectronic traps as fillers significantly enhance breakdown strength and electrostatic energy density of polymer composites. *Compos. Sci. Technol.* **2020**, *195*, 108201.
- (32) Baraskar, B. G.; Kadhane, P. S.; Darvade, T. C.; James, A. R.; Kambale, R. C. BaTiO₃-Based Lead-Free Electroceramics with Their Ferroelectric and Piezoelectric Properties Tuned by Ca²⁺, Sn⁴⁺ and Zr⁴⁺ Substitution Useful for Electrostrictive Device Application. *Ferroelectrics and Their Applications*; IntechOpen, 2018; p 113.
- (33) Li, J.; Zhu, Z.; Fang, L.; Guo, S.; Erturun, U.; Zhu, Z.; West, J. E.; Ghosh, S.; Kang, S. H. Analytical, numerical, and experimental studies of viscoelastic effects on the performance of soft piezoelectric nanocomposites. *Nanoscale* **2017**, *9*, 14215–14228.

(34) Lin, X.; Hu, P.; Jia, Z.; Gao, S. Enhanced electric displacement induces large energy density in polymer nanocomposites containing core-shell structured BaTiO₃@TiO₂ nanofibers. *J. Mater. Chem. A* **2016**, *4*, 2314–2320.

(35) Huang, X.; Sun, B.; Yu, C.; Wu, J.; Zhang, J.; Jiang, P. Highly conductive polymer nanocomposites for emerging high voltage power cable shields: experiment, simulation and applications. *High. Volt.* **2020**, *5*, 387–396.

(36) do Amaral Montanheiro, T. L.; Cristóvan, F. H.; Machado, J. P. B.; Tada, D. B.; Durán, N.; Lemes, A. P. Effect of MWCNT functionalization on thermal and electrical properties of PHBV/MWCNT nanocomposites. *J. Mater. Res.* **2015**, *30*, 55.

(37) Pal, H.; Sharma, V.; Sharma, M. Influence of functionalization on mechanical and electrical properties of carbon nanotube-based silver composites. *Philos. Mag.* **2014**, *94*, 1478–1492.

(38) Ji, X.; Xu, Y.; Zhang, W.; Cui, L.; Liu, J. Review of functionalization, structure and properties of graphene/polymer composite fibers. *Composites, Part A* **2016**, *87*, 29–45.

(39) Pan, Z.; Zhai, J.; Shen, B. Multilayer hierarchical interfaces with high energy density in polymer nanocomposites composed of BaTiO₃@TiO₂@Al₂O₃ nanofibers. *J. Mater. Chem. A* **2017**, *5*, 15217–15226.

(40) Li, J.; Chen, G.; Lin, X.; Huang, S.; Cheng, X. Enhanced energy density in poly(vinylidene fluoride) nanocomposites with dopamine-modified BNT nanoparticles. *J. Mater. Sci.* **2020**, *55*, 2503–2515.